Spatio-temporal profiling of cluster mass fraction in a pulsed supersonic gas jet by frequency-domain holography

Xiaohui Gao,[1,2] Alexey V. Arefiev,[2] Richard C. Korzekwa,[1,2] Xiaoming Wang,[1,2] Bonggu Shim,[1,2] and Michael C. Downer[1,2,a)]
[1]*Department of Physics, The University of Texas at Austin, Austin, Texas 78712, USA*
[2]*Institute for Fusion Studies, The University of Texas at Austin, Austin, Texas 78712, USA*

(Received 14 May 2013; accepted 1 July 2013; published online 19 July 2013)

We present an in-depth study of a rapid, noninvasive, single-shot optical method of determining cluster mass fraction $f_c(\boldsymbol{r}, t)$ at specified positions $\boldsymbol{r}$ within, and at time t after opening the valve of, a pulsed high-pressure pulsed supersonic gas jet. A ~2 mJ, 40 fs pump pulse ionizes the monomers, causing an immediate drop in the jet's refractive index n_{jet} proportional to monomer density, while simultaneously initiating hydrodynamic expansion of the clusters. The latter leads to a second drop in n_{jet} that is proportional to cluster density and is delayed by ~1 ps. A temporally stretched probe pulse measures the 2-step index evolution in a single shot by frequency-domain holography, enabling recovery of f_c. We present a model for recovering f_c from fs-time-resolved phase shifts. We also present extensive measurements of spatio-temporal profiles $f_c(\boldsymbol{r}, t)$ of cluster mass fraction in a high-pressure supersonic argon jet for various values of backing pressure P_0 and reservoir temperature T_0. © *2013 AIP Publishing LLC*. [http://dx.doi.org/10.1063/1.4815961]

I. INTRODUCTION

Interaction of intense laser pulses with clusters containing $N_{\#} > 10^4$ atoms/cluster is of fundamental interest and of practical importance.[1] It has opened up applications for table-top neutron sources,[2,3] electron and ion accelerators,[4–6] and coherent and incoherent X-ray sources.[7–11] Targets comprised of Van-der-Waals bonded clusters formed by condensation in pulsed supersonic gas jets combine advantages of monomer gas targets (extended interaction length, freedom from debris) and solid targets (efficient energy coupling). To fully exploit these benefits, three key properties of the cluster gas target need to be characterized and controlled: the total atomic density N_{tot}, the average cluster size $\bar{r}_c$, and the cluster mass fraction $f_c \equiv N_{\#}N_c/(N_m + N_{\#}N_c)$, where N_c and N_m denote the number density of clusters and monomers, respectively. N_{tot} is straightforwardly determined by interferometry of the neutral jet. Recent advances in tomographic jet characterization enable reconstruction of 3D N_{tot} distributions without assuming cylindrical symmetry.[12] Average cluster radius $\bar{r}_c$ is determined by Rayleigh[13] or Mie[14] scatter measurements and/or estimates based on Hagena's empirical parameter $\Gamma^* = kP_0(0.74d/\tan\alpha)^{0.85}/T_0^{2.29}$ (for monatomic gases),[15] where k is a gas species parameter ($k = 1650$ for argon), P_0 is nozzle backing pressure in mbar, d is the nozzle orifice diameter in μm, α is the expansion half-angle, and T_0 is the gas reservoir temperature in K.

Cluster mass fraction, on the other hand, has proven to be a far more elusive quantity to measure, calculate, or estimate accurately for pulsed supersonic jets typical of intense laser experiments ($\bar{r}_c > 5\,\text{nm}$, $N_{\text{tot}} \sim 10^{18}\,\text{cm}^{-3}$), although various techniques that are restricted to much lower $\bar{r}_c$ and N_{tot}—electron impact ionization/photoionization mass spectroscopy,[16] fluorescence excitation spectroscopy,[17] cluster-helium beam scattering,[18] electron diffraction,[19] surface scattering,[20]—or to molecular gas jets —Raman scattering[21]—have been used to determine f_c in tenuous or molecular clustered gases. While most of the above measurements show substantial presence of unclustered atoms, it is sometimes assumed[22] without clear justification that all atoms in a jet are clustered (i.e., $f_c = 1.0$). On the other hand, theoretical models of cluster nucleation using liquid drop nucleation rate theory,[23] the Smoluchowski coagulation equation,[24] or direct simulation Monte Carlo method[25] show wide variations of f_c in gas jets, typically $f_c < 0.5$ in room temperature jets. Moreover, f_c is often measured on the jet axis far away from the nozzle, while the interaction region in many intense laser-cluster experiments is placed near the edge of a gas jet.[26,27] An *in-situ* characterization is thus required in case f_c varies spatially. f_c also depends on time t after opening the valve, temperature T_0, pressure P_0, and nozzle geometry, although no empirical formulas exist for estimating these dependences. Direct knowledge of f_c is critical not only to the understanding of nucleation and condensation but also to accurate interpretation of a wide variety of laser-cluster experiments including X-ray emission,[28] phase-matched harmonic generation,[26] and ion acceleration,[6] where f_c has not been measured independently. In addition, *in-situ* measurement of $\bar{r}_c$ using Rayleigh scatter[13,29] relies indirectly on knowledge of f_c, since the Rayleigh scatter signal is proportional to $f_c r_c^6$. Direct measurement of $\bar{r}_c$ is needed in many situations where the scaling law using Hagena's parameter is unreliable, including: (i) jets that have not yet reached steady state;[30] (ii) jets with ambiguous nozzle geometric parameters—e.g., a poppet displacement comparable or less than the orifice diameter d may result in a reduced effective throat diameter;[31] or (iii) jets with nozzle shapes

a)Electronic mail: downer@physics.utexas.edu

that do not match the gas flow,[32] or with atypical expansion angle or pressure,[33] where the size deviation is likely caused by the underestimate of jet dimension.[34] These situations illustrate the wide need for an *in-situ* experimental determination of f_c in a high-pressure gas jet containing large clusters. We noted that f_c may also be determined from the scattered light if precise measurements of N_{tot} and $\bar{r}_c$ can be performed without knowing f_c. Unfortunately, except for the Mie scatter regime,[14] optical measurements of $\bar{r}_c$ are coupled with f_c.

In a recent Letter,[35] we reported an *in-situ* method for determining $f_c(\boldsymbol{r},t)$ at position $\boldsymbol{r}$ within, and time t after opening the valve of, a pulsed supersonic jet by measuring femtosecond evolution of the jet's refractive index $n_{\text{jet}}(r,t;\tau)$ by single-shot frequency-domain holography (FDH). Here, τ is the time delay after a focused 2 mJ, 40 fs pump pulse irradiates the jet in the vicinity of $\boldsymbol{r}$ at time t. The pump pulse ionizes both monomers and clusters, with the clusters retaining most of their electrons due to the relatively low pump pulse intensity. Ionization of monomers causes n_{jet} to drop from 1 to $1-\omega_p^2/2\omega_{\text{pr}}^2$ during the pump pulse, where the squared plasma frequency ω_p^2 is proportional to N_m and ω_{pr} is the frequency of the FDH probe pulse. In contrast, the initial cluster contribution to n_{jet} is negligible owing to the high electron density inside each cluster. The pump pulse not only ionizes cluster atoms but also heats the resulting electrons inside clusters, causing clusters to expand hydrodynamically. The electron density inside each cluster decreases as a result of the expansion, and the clusters begin to contribute noticeably to n_{jet} once their internal plasma frequency drops to ω_{pr}.[27,36] The characteristic time scale of the expansion is ~1 ps, during which the supersonic beam travels less than 2 nm.[37] The jet is therefore essentially frozen in time during the evolution of the refractive index caused by cluster expansion. The clusters eventually expand into a uniform monomer plasma, producing a second delayed drop in n_{jet} that is proportional to $N_{\#}N_c$ after approximately 1 ps. Thus, n_{jet} drops in two sequential steps corresponding to monomer and cluster contributions, enabling recovery of f_c. This "2-step" method is well suited for experiments with multi-terawatt fs laser systems, since only a small fraction of the typical pulse energy ($\geq$1 J) of such systems needs to be split off to make the required pump and probe pulses. Moreover, since FDH measures the 2-step drop in n_{jet} in a single shot, spatio-temporal profiles of $f_c(\boldsymbol{r},t)$ and scans of jet parameters (P_0, T_0, α, d) can be carried out quickly to study various influences on cluster fraction.

This paper presents the theory behind the 2-step method and experimental jet profiles and parameter scans in much greater depth than was possible in a Letter. Section II describes the model of monomer and cluster ionization, and of cluster heating and expansion, and relates the measured τ-dependent probe phase shift quantitatively to f_c. Section III describes the experimental procedure in detail and presents extensive measurements of $f_c(\boldsymbol{r},t)$ for clustered argon jets of different reservoir backing pressures and temperatures. Section IV summarizes the conclusions of the study.

II. MODEL OF THE EVOLVING REFRACTIVE INDEX OF AN IONIZED CLUSTER-MONOMER MEDIUM

The time evolution of the refractive index of a cluster-monomer medium contains distinct contributions from clusters and monomers. The monomer contribution to the refractive index appears during the pump pulse and remains constant for the remainder of the measurement interval ($\tau \sim 1$ ps). On the other hand, clusters have to expand significantly to contribute noticeably to the refractive index. For our experimental parameters, the characteristic time required for the cluster contribution to reach its asymptotic value is roughly 1 ps, significantly longer than the duration of the pump pulse (40 fs). In this section, we formulate a model for evaluating monomer and cluster contributions that then allows us to extract the cluster mass fraction f_c from the measured phase shifts.

A. Monomer contribution

The density of ions with charge state Z, $N_{\text{mi}}(Z)$, evolves in the monomer gas irradiated by the pump pulse according to the equation

$$\frac{dN_{\text{mi}}(Z)}{d\tau} = -W_m(Z)N_{\text{mi}}(Z) + W_m(Z-1)N_{\text{mi}}(Z-1), \quad (1)$$

where $W_m(Z)$ is the ionization rate from charge state Z to charge state $Z+1$. The characteristic ion density is the density of the monomer gas N_m, typically less than $10^{19}\,\text{cm}^{-3}$. Thus, the collisional ionization rate is significantly lower than the rate of ionization directly by the laser field. Therefore,

$$W_m(Z) = W_{\text{ADK}}(Z) = \frac{1}{2l+1}\sum_{m=-l}^{l} w_{\text{ADK}}(n^*,l,m), \quad (2)$$

where $W_{\text{ADK}}(Z)$ is the tunnel ionization rate from a charge state Z to $Z+1$ averaged over the magnetic quantum number m, l is the angular momentum quantum number, n^* is the effective principal quantum number, and w_{ADK} is the rate given by the cycle-averaged Ammosov-Delone-Krainov (ADK) formula[38]

$$w_{\text{ADK}}(n^*,l,m) = \frac{1}{2}\omega_a C_{n^*l}^2 f(l,m)\frac{I_p}{I_H}\left(\frac{3}{\pi}\chi\right)^{1/2} \times \left(\frac{2}{\chi}\right)^{2n^*-|m|-1}\exp\left(-\frac{2}{3\chi}\right), \quad (3)$$

where

$$C_{n^*l} \equiv \left(\frac{2\exp(1)}{n^*}\right)^{n^*}\frac{1}{\sqrt{2\pi n^*}}, \quad (4)$$

$$f(l,m) \equiv \frac{(2l+1)(l+|m|)!}{2^{|m|}|m|!(l-|m|)!}, \quad (5)$$

$$\chi \equiv \frac{E_{\text{ext}}}{E_a}\left(\frac{I_p}{I_H}\right)^{-3/2}. \quad (6)$$

In Eqs. (3)–(6), I_p is the ionization potential from a charge state Z to $Z+1$ in eV, E_{ext} is the electric-field envelope of

the laser pulse in V/cm, $\omega_a = 4.1341 \times 10^{16}\,\mathrm{s}^{-1}$ is the atomic frequency unit, $I_H = 13.6\,\mathrm{eV}$ is the ionization potential of hydrogen, $E_a = 5.142 \times 10^9\,\mathrm{V/cm}$ is the atomic unit of electric-field strength, $n^* = Z\sqrt{I_p/I_H}$, l depends on the subshell of electron to be ionized (e.g., $l=0$ for s electrons and $l=1$ for p electrons), m is an integer between $-l$ and l.

For a given $E_{\mathrm{ext}}(t)$, Eq. (1) determines the time evolution of $N_i(Z)$, provided initially $N_i(0) = N_m$ and $N_i(Z) = 0$ for other Z's. The average charge state of the monomer medium is defined in terms of the ion density as

$$Z_m \equiv \sum_{Z=0}^{\infty} Z N_{\mathrm{mi}}(Z) \Big/ \sum_{Z=0}^{\infty} N_{\mathrm{mi}}(Z), \tag{7}$$

where $\sum_{Z=0}^{\infty} N_{\mathrm{mi}}(Z) = N_m$. The monomer ionization level in this model rapidly increases during the laser pulse and remains constant after the pulse. Here, we neglect three body recombination because the characteristic time for this process at typical monomer densities is much longer than the time interval of interest, which is the cluster expansion time.

Figure 1 shows the asymptotic monomer charge state Z_m calculated using Eqs. (1)–(7) for a range of intensities and pulse durations. In our experiments, we used an 800 nm, 40 fs FWHM Gaussian pulse with peak intensity $I_{\mathrm{pu}} = 4 \times 10^{14}\,\mathrm{W/cm^2}$, so that the monomer ionization level is $Z_m \approx 1$, and is insensitive to small errors in I_{pu}.

The refractive index of the resulting tenuous plasma for a probe pulse of frequency ω_{pr} is

$$n_{\mathrm{pl}} \approx 1 - \omega_p^2/2\omega_{\mathrm{pr}}^2, \tag{8}$$

where $\omega_p = \sqrt{4\pi Z_m N_m e^2/m_e}$ is the plasma frequency, with e the electron charge and m_e the electron mass. Hence, the change of the refractive index caused by the ionization of monomers is

$$\Delta n_m = n_{\mathrm{pl}} - 1 = -Z_m N_m / 2N_{\mathrm{crit}}, \tag{9}$$

where $N_{\mathrm{crit}} = m_e\omega_{\mathrm{pr}}^2/4\pi e^2$ is the critical density of the probe pulse. Δn_m depends only on one unknown parameter N_m, since both N_{crit} and Z_m are known for a given pump pulse.

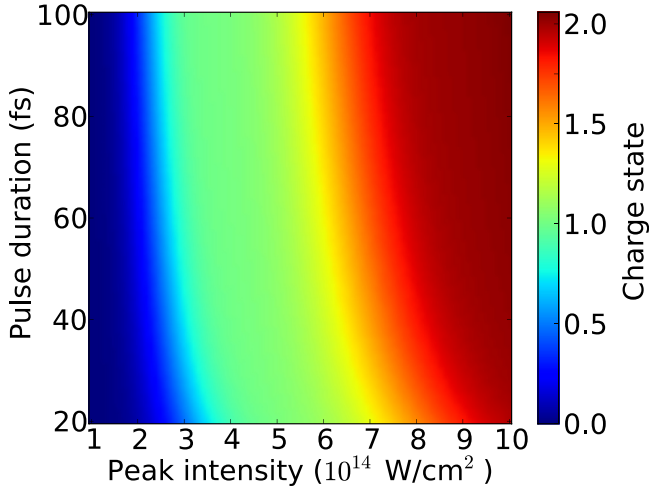

FIG. 1. Charge state of a monomer argon medium as a function of peak-intensity and pulse duration (FWHM) of an 800 nm Gaussian pulse.

Equation (9) neglects the change of the refractive index associated with bound electrons, Δn_b. In the case of ionization from Ar to Ar^+, the ratio of the index change contributed by bound electrons to that by free electrons is $4\pi(\alpha_{\mathrm{ArI}} - \alpha_{\mathrm{ArII}})N_{\mathrm{crit}}$, which is 0.05 at 400 nm. Here, α_{ArI} is the polarizability of a neutral argon atom and $\alpha_{\mathrm{ArII}} \approx 0.65\alpha_{\mathrm{ArI}}$ is the polarizability of a singly ionized argon atom.[39] The ratio is even lower when the neutral atom is ionized to higher charge states. Therefore, Δn_b can be safely neglected.

B. Cluster contribution

The asymptotic change to the refractive index for the probe pulse due to clusters is given by an equation analogous to that for monomers [see Eq. (9)]

$$\Delta n_c = -Z_c N_{\#} N_c / 2N_{\mathrm{crit}}, \tag{10}$$

where Z_c is the asymptotic average charge state of the cluster medium after all clusters fully expand. The goal of the model developed in the following two sub-sections is to determine Z_c. The cluster expansion is triggered by the pump pulse. Since the expansion time for a typical cluster (~ps) significantly exceeds the duration of the pump pulse (~40 fs), cluster expansion can be neglected during the interaction with the laser. Therefore, we use a two-stage model,[36,40] where cluster ionization/heating and cluster expansion are treated sequentially. Once Z_c is determined, Δn_c becomes a function of only one unknown parameter, $N_{\#}N_c$, the average number density of atoms initially contained by clusters.

1. Cluster ionization and heating

We assume that initially a cluster is a uniform sphere of atoms at solid density, the radius of which is much less than the wavelength of the pump pulse. Since we neglect the expansion, cluster interaction with the pump pulse effectively becomes a zero-dimensional problem. A particle balance equation for ions has to be solved together with an energy balance equation for free electrons. In what follows, we present a comprehensive model of cluster ionization and heating that includes a number of relevant processes. Their relative importance is examined for our specific laser parameters after the model is formulated.

The time evolution of the ion density $N_{\mathrm{ci}}(Z)$ and electron temperature T_e follow the equations

$$\begin{aligned}\frac{dN_{\mathrm{ci}}(Z)}{d\tau} = &-[W_c(Z) + \alpha_3(Z)N_e^2]N_{\mathrm{ci}}(Z) \\ &+ W_c(Z-1)N_{\mathrm{ci}}(Z-1) \\ &+ \alpha_3(Z+1)N_e^2 N_{\mathrm{ci}}(Z+1),\end{aligned} \tag{11}$$

$$\begin{aligned}\frac{dT_e}{d\tau} = &\frac{2}{3}\frac{Q}{N_e} - \frac{T_e}{N_e}\frac{dN_e}{dt} + \frac{2}{3N_e}\sum_{Z=0}^{\infty}\varepsilon(Z) \\ &\times [\alpha_3(Z+1)N_e^2 N_{\mathrm{ci}}(Z+1) - W_{\mathrm{eii}}^{\mathrm{cl}} N_{\mathrm{ci}}(Z)],\end{aligned} \tag{12}$$

where $N_e = \sum_{Z=0}^{\infty} Z N_{\mathrm{ci}}(Z)$ is the electron density, $W_c(Z)$ is the total ionization rate from a charge state Z to a charge

state $Z+1$, α_3 is the three body recombination rate, Q is the inverse bremsstrahlung (IBS) (or collisional) energy absorption rate, $\varepsilon(Z)$ is the ionization potential of an ion with charge state Z, and $W_{\rm coll}^{\rm th}$ is the rate of collisional ionization by thermal electrons. Equation (11) should be solved for every charge state.

The total ionization rate $W_c(Z)$ in Eq. (11) is a sum

$$W_c(Z) = W_{\rm ADK}(Z) + W_{\rm coll}^{\rm th}(Z) + W_{\rm coll}^{\rm las}(Z), \qquad (13)$$

of field (ADK) and collisional (coll) ionization rates. The tunneling ionization rate $W_{\rm ADK}$ is given by Eqs. (2)–(6), except that instead of the external field $E_{\rm ext}$ we should use the screened field $E_c = 3E_{\rm ext}/|\epsilon_c + 2|$ inside the cluster with dielectric constant $\epsilon_c = 1 + 4\pi N_{\rm ci}(0)\alpha_{\rm I}[1 - 4\pi N_{\rm ci}(0)\alpha_{\rm I}/3]^{-1} - \omega_p^2/[\omega(\omega + i\nu)]$. Here, $N_{\rm ci}(0)$ is the density of neutral atoms, $\alpha_{\rm I}$ is the atomic polarizability, and ν is collision frequency. We have assumed that the cluster is spherical, uniform, and small enough that it experiences an essentially uniform laser field. $W_{\rm coll}^{\rm las}$ is a correction to $W_{\rm coll}^{\rm th}$ caused by electron quiver motion in the laser field, which can be considerable for our conditions. We calculate the thermal contribution to the collisional ionization rate using the expression

$$W_{\rm coll}^{\rm th} = N_e S \exp\left(-\frac{\Delta\varepsilon}{T_e}\right), \qquad (14)$$

where S is the collisional ionization rate given by the Lotz formula,[41] assuming a Maxwellian distribution with temperature T_e, and $\Delta\varepsilon(Z, T_e, N_e)$ is the shift of the ionization energy[42,43] caused by plasma screening. We approximate the additional contribution from quiver motion by $W_{\rm coll}^{\rm las} = W_{\rm las}\exp(-\Delta\varepsilon/T_e)$, where $W_{\rm las}$ is the collisional ionization rate used in Refs. 44 and 45. The three body recombination rate in Eq. (11) and (12) is[46]

$$\alpha_3 = \frac{4\pi\sqrt{2\pi}}{9}\frac{e^{10}Z^3}{m_e^{1/2}T_e^{9/2}}\ln\sqrt{1+Z^2}. \qquad (15)$$

The IBS absorption rate for a uniform spherical plasma is given by[43]

$$Q = \frac{\omega_p^2\nu}{(\omega - \omega_p^2/3\omega)^2 + \nu^2}\frac{|E_{\rm ext}|^2}{8\pi}. \qquad (16)$$

Because the plasma is of solid density and the temperature is not high, the collision frequency ν is evaluated using an interpolation formula suited for warm dense matter[47,48]

$$\nu \simeq 2\sqrt{2\pi}\frac{Ze^4N_e}{m_e^{1/2}T_e^{3/2}} \times \ln\left(1 + \frac{1.32}{\sqrt{2\pi}}\frac{T_e}{(m_e^{1/2}Ze^2\tilde{\omega})^{2/3}}\right)F(T_e, \hbar\omega), \qquad (17)$$

where $\tilde{\omega} = \max(\omega, \omega_p)$ and $F(T_e, \hbar\omega)$ is the Fermi factor.

We have solved the system of ordinary differential equations (ODEs) (11) and (12) numerically using a Runge-Kutta solver. The required initial conditions are the atomic density $N_{\rm ci0}(0)$ and initial electron temperature T_{e0}. We obtained $N_{\rm ci0}(0) = 2.63 \times 10^{22}$ cm^{-3} using the lattice constant of argon clusters $a_{\rm Ar} = 0.534 \pm 0.001$ nm with fcc structure.[49,50] It is not possible to directly set T_{e0} to zero. However, the result of the calculations should not depend on the value of T_{e0} if it is sufficiently low. We have directly verified that setting $T_{e0} = 2$ eV ensures that the initial temperature is effectively zero in the context of the final result. After $N_{\rm ci}(Z)$ is determined, the average charge state inside the cluster is calculated by

$$Z_c \equiv \sum_{Z=0}^{\infty} ZN_{\rm ci}(Z) \Big/ \sum_{Z=0}^{\infty} N_{\rm ci}(Z). \qquad (18)$$

Evolution of Z_c and T_e for five versions of the described model is shown in Fig. 2. In the simplest version ((1), dashed black curves), equivalent to the nanoplasma model of Ref. 44, continuum lowering, recombination, and the influence of changing N_e on T_e are neglected, and thus IBS is the only source for temperature evolution. For remaining versions, neglected terms were restored successively, with each version retaining all elements of the previous version: (2) lowering of ionization potential (short-dashed blue curves); (3) effect of recombination on N_e (dashed-dotted red curves); (4) influence of changing N_e on T_e (dashed-dotted-dotted purple curves); (5) influence of recombination and collisional ionization on energy loss/gain (solid green curves). Of the four modifications (versions 2–5) of the nanoplasma model,[44] inclusion of three-body recombination on N_e is the most important one. Recombination balances collisional ionization, resulting in a constant Z_c after the laser pulse passes. In addition, Z_c is substantially lowered and T_e is increased. Since Z_c and T_e do not evolve after $\tau = 40$ fs, we choose values thereafter as the initial conditions for the expansion model.

The charge state after ionization and heating is shown in Fig. 3 as a function of peak laser intensity and pulse duration. Compared to Fig. 1, which features broad plateaus of integer charge state Z_m separated by narrow steps of fractional charge state, Fig. 3 features broad regions of fractional charge state Z_c and an overall smoother growth of Z_c with $I_{\rm pu}$ (except at low $I_{\rm pu}$). This difference is attributable to the dominance of tunnel ionization in the former case, and collisional ionization in the latter. In our model, ionization and heating are size-independent, so that each cluster in a size-dispersed

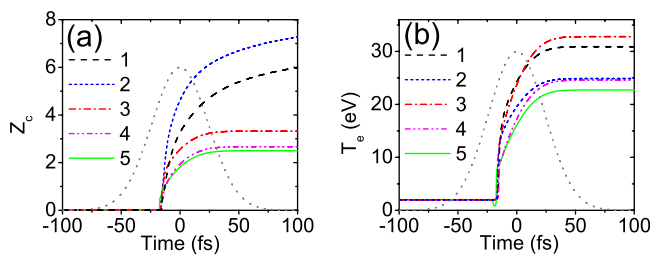

FIG. 2. Calculated time evolution of Z_c (left) and T_e (right) in a cluster exposed to 40 fs, 800 nm pulse with peak intensity 4×10^{14} W/cm^2, for 5 versions of the cluster ionization/heating model. Modifications to the model were added successively. (1) nanoplasma model (no expansion), (2) lowering of ionization potential, (3) recombination, (4) change of T_e due to change of N_e, (5) energy loss/gain due to recombination and collisional ionization. The dotted grey line shows the electric-field envelope.

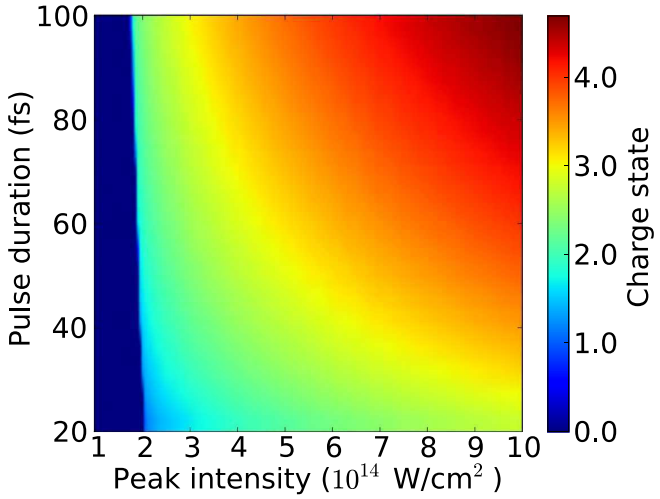

FIG. 3. Average charge state inside the cluster after ionization and heating as a function of peak-intensity and pulse duration (FWHM) of an 800 nm Gaussian pulse based on version 5 of the model. Values are extracted at $\tau = 1.2\tau_p$, where τ_p is the pulse duration.

ensemble irradiated by the same pump pulse would reach the same charge state. For a 40 fs FWHM Gaussian pulse with $I_{pu} = 4 \times 10^{14}$ W/cm^2, the average charge state and electron temperature after ionization and heating are $Z_c = 2.50$ and $T_e = 22.7$ eV.

We have benchmarked our model against a 3D microscopic particle-in-cell (MPIC) code[51] at three peak intensities for 800 nm, 100 fs laser pulses. Table I presents a comparison of Z_c obtained from the MPIC code and Z_c calculated using our model. The difference between the results for our most accurate model (version 5) and those from MPIC simulations is less than 20%, which indicates that our model includes the key physics processes. Considering its significantly lower cost in computational time and resources, our model is better suited to interpret laser-cluster experiments when only macroscopic characteristics like Z_c are required for a wide range of parameters.

2. Cluster expansion

Cluster interaction with the pump pulse considered in Sec. II B 1 produces a spherical quasineutral plasma of radius r_c. We assume that electron temperature, density, and the ion charge state (for all Z's) are initially uniform throughout the cluster. The electron pressure causes the cluster with these initial parameters to expand. To describe this expansion, we use a simplified model that assumes that electrons are isothermal and treats ions as a fluid. The model accounts for the change in the number of ions with charge state Z in each fluid element due to collisional ionization and three body recombination. The model consists of momentum, particle, and energy balance equations

$$\frac{du}{d\tau} = -\left(\sum_{Z=0}^{\infty} N_{ci}(Z)\right)^{-1} \frac{T_e}{m_i}\frac{\partial N_e}{\partial r}, \tag{19}$$

$$\frac{\partial N_{ci}(Z)}{\partial \tau} + \frac{1}{r^2}\frac{\partial}{\partial r}\left[uN_{ci}(Z)r^2\right] = -J, \tag{20}$$

$$\frac{d}{d\tau}\left[\frac{3}{2}T_e\int N_e r^2 dr + \int r^2 dr\left(\frac{m_i}{2}u^2\sum_{Z=1}^{\infty} N_{ci}(Z)\right)\right] = \int r^2 dr\left(\sum_{Z=0}^{\infty}\varepsilon_i(Z)\alpha_3(Z+1)N_e^2 N_{ci}(Z+1) - \varepsilon_i(Z)W_{coll}^{th}(Z)N_{ci}(Z)\right), \tag{21}$$

where u is the flow velocity, $N_e \equiv \sum_{Z=0}^{\infty} ZN_{ci}(Z)$ is the electron density, and m_i is the ion mass. The source term

$$J = [W_{coll}^{th}(Z) + \alpha_3(Z)N_e^2]N_{ci}(Z) - W_{coll}^{th}(Z-1)N_{ci}(Z-1) - \alpha_3(Z+1)N_e^2 N_{ci}(Z+1) \tag{22}$$

on the right hand-side of Eq. (20) accounts for collisional ionization, the rate W_{coll}^{th} of which is given by Eq. (14), and for three body recombination, the rate of which is given by Eq. (15). The right-hand side of Eq. (21) is the energy change of the electron population caused by these same two processes. Equation (20) should be solved for each charge state Z. In this model, the flow velocity and electron and ion densities are functions of radius r and time τ, whereas the electron temperature T_e is only a function of time.

Equations (19)–(21) can be solved numerically using a Lagrangian solver with a staggered radial grid to obtain N_i, u, and T_e, taking as initial conditions $u = 0$ with initial ion charge state distribution $N_{i0}(Z)$, average charge state Z_{c0},

TABLE I. Comparison of Z_c in Ref. 51 to Z_c computed by version 1 and version 5 of our model at $\tau = 120$ fs for 100 fs pump pulses.

	Charge state Z_c		
Intensity (W/cm^2)	MPIC	Version 1	Version 5
1×10^{15}	5.63	7.80	4.69
3×10^{15}	6.80	8.37	6.41
1×10^{16}	7.52	10.2	8.20

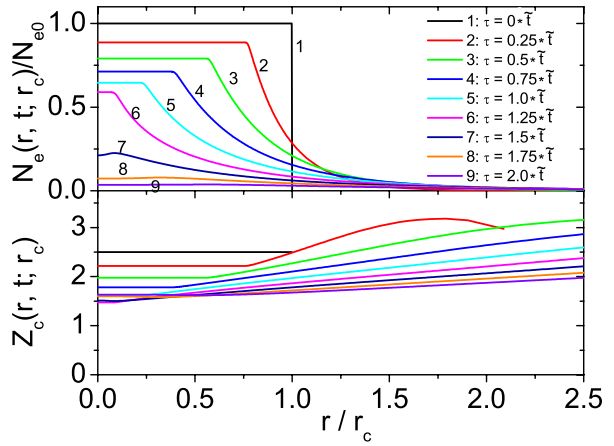

FIG. 4. Snapshots of electron density and charge state during expansion of a cluster with initial radius 7 nm. The initial conditions are created by a 40 fs pulse with peak intensity $I_{pu} = 4 \times 10^{14}$ W/cm^2. The legend gives the times of each snapshot in terms of the characteristic expansion time $\tilde{t} = r_c/C_{s0}$, where C_{s0} is the initial sound speed. In units of fs these times are (1) 0, (2) 150, (3) 299, (4) 449, (5) 598, (6) 748, (7) 897, (8) 1047, (9) 1197.

electron density N_{e0}, and electron temperature T_{e0} input from the model for ionization and heating of Sec. II B 1. The average charge state now develops radial dependence, which can be calculated using Eq. (18) for given radial profiles $N_i(Z)$. As an example, Fig. 4 shows snapshots of normalized electron density $N_e(r)/N_{e0}$ and charge state $Z_c(r)$ distributions within a cluster calculated for excitation by a 40 fs pulse with peak intensity $I_{pu} = 4 \times 10^{14}\,\mathrm{W/cm^2}$. The snapshots are shown for various multiples of the characteristic expansion time $\tilde{t} = r_c/C_{s0}$, where $C_{s0} = \sqrt{Z_{c0}T_{e0}/m_i}$ is the initial speed of sound. The solid blue curves in Figs. 5 and 6(a) show, respectively, the time evolution of $Z_c(t)$ averaged over the cluster and the electron temperature $T_e(t)$. For this excitation, the initial conditions from Sec. II B 1 were $Z_{c0} = 2.50$, $T_{e0} = 22.7$ eV and $N_{i0}(Z)$ shown by blue bars in Fig. 6(b).

As the cluster begins to expand at the edge, the electrons begin to cool, transferring their energy to ions. Figure 4 shows a rarefaction wave that propagates inwards. Before the rarefaction wave reaches the center of the cluster, the ion density there remains constant. The temperature decrease, however, tips the initial balance between collisional ionization and recombination in favor of recombination. The resulting recombination causes N_e and Z_c to decrease simultaneously near the center of the cluster (see Fig. 4). Close to the edge of the cluster the situation is the exact opposite. The sharp decrease in ion density due to expansion tips the balance between collisional ionization and recombination in favor of ionization. Thus at early times, Z_c *increases* near the cluster edge, resulting in a $Z_c(r)$ profile that increases with r. Despite these dynamics, the average Z_c over the entire cluster changes by only ~10% (from 2.50 to 2.24) over 1.5 ps, as shown by the solid blue curve in Fig. 5. This remains true at lower I_{pu} (and thus lower T_{e0}), as shown by the dashed red curve in Fig. 5 for a cluster ionized and heated to $Z_{c0} = 1.56$, $T_{e0} = 13.6\,\mathrm{eV}$ by a 40 fs pump pulse with $I_{pu} = 2 \times 10^{14}\,\mathrm{W/cm^2}$.

Evidently, the inclusion of recombination during the expansion does not critically affect the average asymptotic charge state of the cluster. However, the recombination is essential for determining the time evolution of electron temperature. As shown in Fig. 6(a), the temperature decreases rapidly if the recombination is not included. Figure 6(b) shows the charge state distribution before the expansion and at $\tau = 1.5$ ps with the recombination included. The relatively slow temperature decrease in Fig. 6(a) for the case with the recombination included is due to the energy release from recombination of Ar^{3+}. The time evolution of electron temperature affects the electron-ion collision frequency and, consequently, it affects the energy that an expanding cluster can absorb if irradiated by a low-intensity probe pulse. The energy absorption of a probe pulse can be used to determine the cluster-size distribution,[36] and in this case the inclusion of recombination (as in the model presented in this section) can have a significant impact on the result.

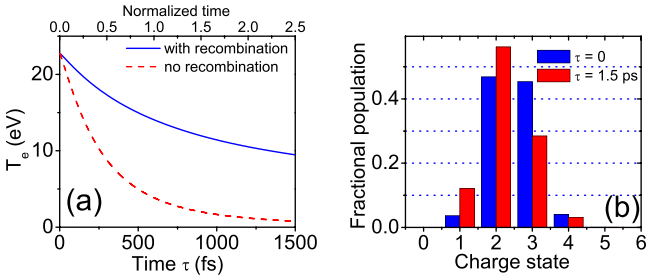

FIG. 6. (a) Evolution of electron temperature during an isothermal expansion of a 7 nm cluster with recombination and ionization included (solid line) and without these processes (dashed line). (b) Charge state distribution at $\tau = 0$ and $\tau = 1.5$ ps.

C. Evaluation of f_c from phase shifts

The asymptotic values of Z_m and Z_c are sufficient to determine the cluster fraction. However, once the time evolution of the ion density profile has been calculated for the monomer and cluster medium, one can determine the time evolution of the refractive index of the cluster-monomer medium using the procedure described in Ref. 36. A result of such calculation is shown in Fig. 7 (solid red curve) for a gas jet with cluster size $r_c = 7$ nm and cluster mass fraction $f_c = 0.35$ irradiated by an 800 nm, $4 \times 10^{14}\,\mathrm{W/cm^2}$, 40 fs

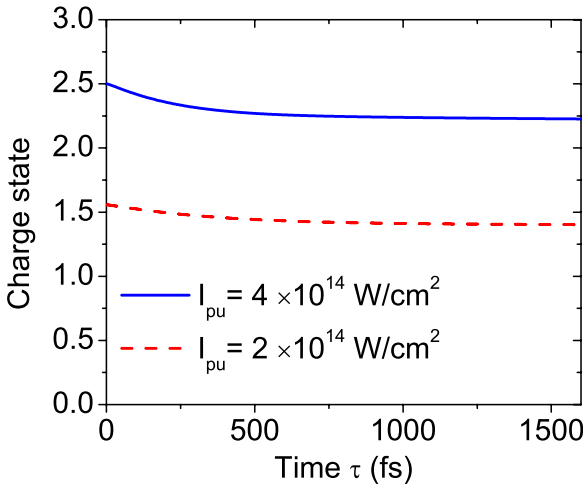

FIG. 5. Evolution of Z_c during the expansion of a 7 nm cluster subjected to a 40 fs, 800 nm pulse for two peak intensities.

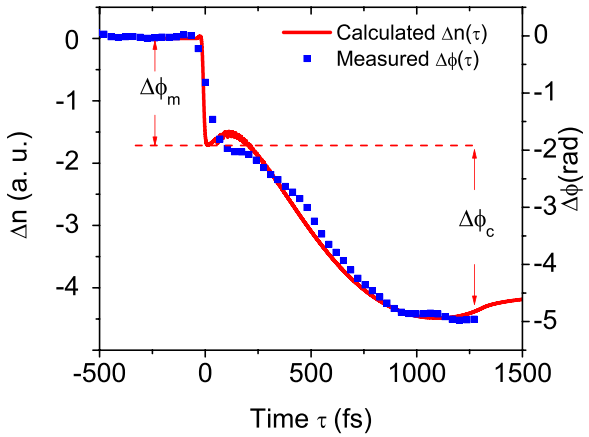

FIG. 7. Measured time-dependent probe phase shift (blue squares) and computed refractive index change (red curve) along the propagation axis of an intense (4×10^{14} W/cm^2), ultrashort (40 fs) pulse after it ionizes monomers and clusters at $\tau = 0$.

laser pulse. For comparison, the blue squares are the time-resolved phase shifts along the propagation axis measured in the experiment described in the next section, and the average cluster size is $\bar{r}_c = 6 \pm 1$ nm determined by transverse interferometry, Rayleigh scatter,[13] and the knowledge of f_c. Figure 7 illustrates how the phase shift evolves in time in two distinct successive stages: a rapid drop corresponding to a monomer contribution and gradual decrease resulting from cluster expansion. The asymptotic contributions from monomers and clusters are indicated by $\Delta\phi_m$ and $\Delta\phi_c$.

The probe phase shift is related to the change of refractive index Δn by

$$\Delta\phi_{\mathrm{pr}} = \frac{2\pi}{\lambda_{\mathrm{pr}}} \int \Delta n(z)\, dz, \tag{23}$$

where λ_{pr} is the wavelength of the probe pulse and z denotes the distance from the entrance of the gas jet. Using $N_m(z) = [1 - f_c(z)]N_{\mathrm{tot}}(z)$ and Eq. (9), we obtain

$$\Delta n_m(z) = -\frac{Z_m[1 - f_c(z)]N_{\mathrm{tot}}(z)}{2N_{\mathrm{crit}}}. \tag{24}$$

Hence,

$$\Delta\phi_m = -\frac{\pi}{\lambda_{\mathrm{pr}}}\frac{Z_m}{N_{\mathrm{crit}}} \int [1 - f_c(z)]N_{\mathrm{tot}}(z)\, dz. \tag{25}$$

Similarly, using $N_{\#}N_c = f_c(z)N_{\mathrm{tot}}(z)$ and Eq. (10), we obtain

$$\Delta n_c(z) = -\frac{Z_c f_c(z)N_{\mathrm{tot}}(z)}{2N_{\mathrm{crit}}}. \tag{26}$$

Hence,

$$\Delta\phi_c = -\frac{\pi}{\lambda_{\mathrm{pr}}}\frac{Z_c}{N_{\mathrm{crit}}} \int f_c(z)N_{\mathrm{tot}}(z)\, dz. \tag{27}$$

We define an average cluster fraction

$$\bar{f}_c \equiv \frac{\int f_c(z)N_{\mathrm{tot}}(z)\, dz}{\int N_{\mathrm{tot}}(z)\, dz}. \tag{28}$$

The following expression is obtained using Eqs. (25) and (27):

$$\bar{f}_c = \frac{Z_m\Delta\phi_c}{Z_c\Delta\phi_m + Z_m\Delta\phi_c}, \tag{29}$$

which allows us to determine the average cluster fraction from the observables $\Delta\phi_m$ and $\Delta\phi_c$ and calculated asymptotic Z_m and Z_c.

III. EXPERIMENT AND RESULTS

A. Experimental setup

In our experiments, a General Valve series 9 solenoid valve regulated supersonic gas flow emerging from a conical nozzle (orifice diameter $d = 760\,\mu$m, half angle $\alpha = 9^\circ$) backed by high pressure (14–40 bar) argon gas at room temperature. A base vacuum of 6×10^{-4} Torr was maintained by a turbo pump with no gas load present. The repetition rate of the gas jet was reduced to 0.25 Hz, ensuring a background pressure $P_b < 1 \times 10^{-3}$ Torr during the firing of the gas jet. The ionization of residual atoms has no observable contribution to the phase shift. An Iota One valve driver (General Valve) controlled the opening time of the valve and the delay t between the laser and the firing of the gas jet. The transverse position of the gas jet x, defined as the distance from jet axis to the laser axis, was adjusted using a translation stage. A series-99 valve sealed by a metal gasket was used at low temperature. A copper block closely surrounding the valve body acted as a temperature reservoir. Nitrogen gas, pre-cooled by liquid nitrogen, flowed through and cooled the block. A type-T thermocouple attached to the block measured its temperature.

A train of 800 nm, 40 fs pulses from a 10 Hz Ti:S laser system was divided into two parts. One served as the pump; the other was frequency-doubled in a 500 μm potassium dihydrogen phosphate (KDP) crystal and split by a Michelson interferometer into probe and reference pulses. The probe and reference pulses, separated by 3 ps, were chirped to ~2 ps duration in a 2 cm SF10 glass, and apertured by an iris of ~1mm diameter to ensure a large spot with uniform wavefront at the focus. These 400 nm pulses and the 800 nm pulses co-propagated after recombination at a dichroic beam splitter. The three pulses were focused by an off-axis parabola ($f^{\#} \approx 60$ for pump) through the gas jet. Reference and probe pulses, frequency filtered by a dichroic beam splitter and a BG39 glass filter, were imaged to the entrance slit of an imaging spectrometer (Jobin Yvon HR460). By imaging a mesh 2 mm behind the jet axis, we ensured that the object plane of the imaging system was at the exit of the gas jet. A 12-bit CCD camera recorded the frequency-domain hologram formed by the reference and probe pulses at the spectrometer's detection plane.

B. Time-resolved phase shift

The lower right portion of Fig. 8 shows a typical two-dimensional hologram recorded in a single shot. The structure along the wavelength axis encodes the spectral phase shift $\Delta\phi(\omega)$ and amplitude $E_{\mathrm{pr}}(\omega)$ that can be extracted from the hologram using a Fourier transform procedure.[52] The temporal phase shift is then reconstructed from the spectral phase and spectral amplitude of both the probe and reference pulses.[53,54] Figure 9 shows a reconstructed single-shot temporal probe phase shift $\Delta\phi_{\mathrm{pr}}(x', \tau)$ as a function of time τ behind the pump pulse and distance x' from its propagation axis.

A line-out of the phase shift from Fig. 9 along the laser axis gives a curve similar to that shown in Fig. 7. The curve has two distinct segments, which allows us to determine the monomer contribution $\Delta\phi_m$ and cluster contribution $\Delta\phi_c$ to the phase shift. The knowledge of Z_m and Z_c is required in order to calculate the cluster mass fraction $\bar{f}_c$ using Eq. (29). Both quantities depend on the local intensity of the pump pulse. In Fig. 10(a), we have plotted the asymptotic values of

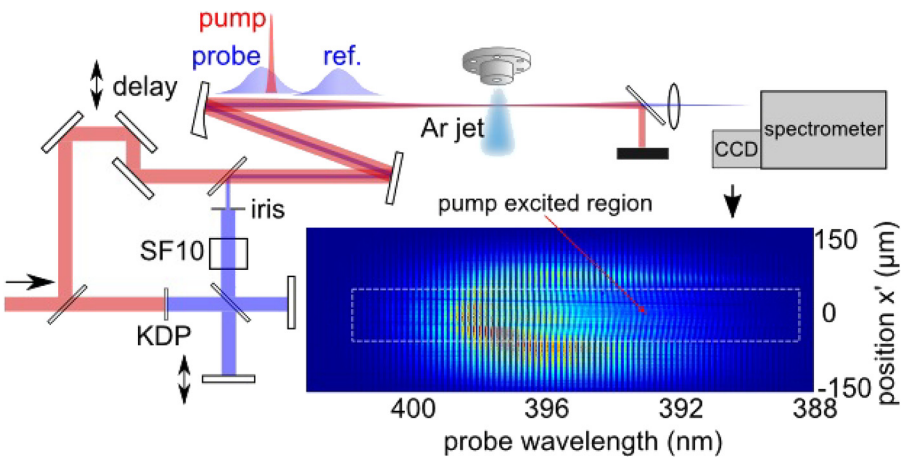

FIG. 8. Schematic of FDH experiment that measures fs-time-resolved refractive index $n_{\text{jet}}(\tau)$ of a cluster gas jet in a single shot.

Z_m and Z_c for a range of laser intensities using the most complete version 5 of the ionization/heating model and expansion model of Sec. II. In our experiments, we specifically choose the pump pulse parameters such that the intensity on axis is $I_{\text{pu}} = 4 \times 10^{14}\,\text{W/cm}^2$. The monomer charge state Z_m has a plateau at this intensity, which minimizes the sensitivity of the result to small uncertainties in I_{pu}. At $I_{\text{pu}} = 4 \times 10^{14}\,\text{W/cm}^2$, we have $Z_m = 1$ and $Z_c = 2.24$ [see Fig. 10(a)]. The measured phase shift contributions along the laser axis in Fig. 9 are $\Delta\phi_m = 1.05$ and $\Delta\phi_c = 0.95$ and the resulting cluster mass fraction that follows from Eq. (29) is $\bar{f}_c = 0.29$.

The intensity of the pump pulse was determined *in-situ* by measuring the ionization threshold for the monomers. As shown in Fig. 10(a), there is an intensity threshold at $I_{\text{pu}} = 1.9 \times 10^{14}\,\text{W/cm}^2$ below which the monomers are not ionized and thus do not contribute to the phase shift. We have measured the phase shift produced by monomers for different laser energies at $t = 0.3$ ms after firing the gas jet, before clusters have formed, as discussed below. The results of this scan are shown in Fig. 10(b), where the red curve is a 10-point Savitzky-Golay smoothing curve. The energy was tuned by a $\lambda/2$ plate and a thin film polarizer. A photodiode recorded the energy leaking through a dielectric mirror for each shot. The scan allowed us to determine the threshold energy, $E = 0.8$ mJ, at which the phase shift appears and which corresponds to the threshold intensity $I_{\text{pu}} = 1.9 \times 10^{14}\,\text{W/cm}^2$. The laser intensity doubles at twice this energy, which corresponds $I_{\text{pu}} = 4 \times 10^{14}\,\text{W/cm}^2$. We choose this energy in our experiments to ensure that the laser intensity is around the plateau of Z_m.

There is a well pronounced transverse variation of the phase shift in Fig. 9. This variation is caused by an intensity variation at the pumped region sampled by the spectrometer slit rather than by variations of the gas jet parameters, because variation of f_c and N_{tot} across the focal spot is negligible. Figure 11 shows the measured monomer (black squares) and cluster (red circles) contributions to the phase shift as a function of distance from the pump propagation axis. Assuming gas jet parameters are constant on this spatial scale, Eq. (25) shows that $\Delta\phi_m = CZ_m$, where C is a constant that is independent of distance from the axis. Since $\Delta\phi_m = 1.05$ and $Z_m = 1$ on the axis, we then have $\Delta\phi_m = 1.05Z_m$ at all positions within the pump focus. The plotted values of $\Delta\phi_m$ (black squares) in Fig. 11 thus mimic the radial profile of Z_m, from which we can recover the radial profile of the laser intensity. The result is nearly a Gaussian profile with spot size $w_0 = 42\,\mu$m. The blue curve in Fig. 11 shows the $\Delta\phi_m$ profile calculated for such a Gaussian, the radial intensity values of which are shown along the upper horizontal axis of Fig. 11. We can now use the radial intensity profile to also find a radial profile of Z_c using its plotted values from Fig. 10(a). Since Eq. (27) shows that $\Delta\phi_c = C'Z_c$, where C' is also a constant, we can use the measured value of $\Delta\phi_c$ and the calculated value of Z_c on the axis to deduce the radial profile of $\Delta\phi_c$. This phase shift agrees well with the

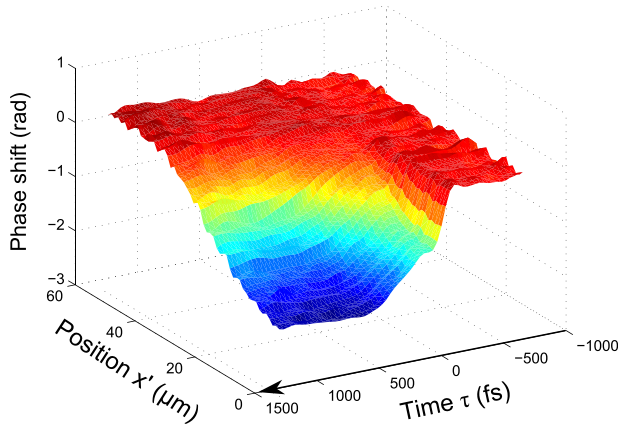

FIG. 9. Time-resolved phase shift $\Delta\phi_{\text{pr}}(x', \tau)$ after the laser pulse ionizes the gas jet at $\tau = 0$. Here, x' is the distance from the laser propagation axis.

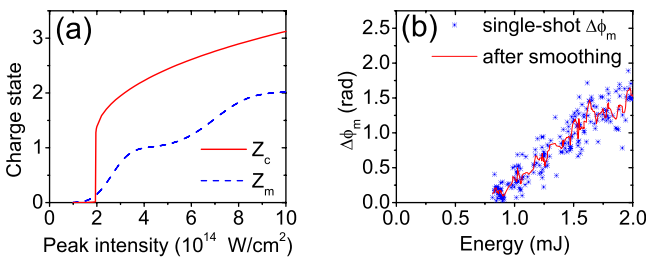

FIG. 10. (a) Asymptotic charge state of Ar clusters (solid red) and monomers (dashed blue) calculated for an 800 nm, 40 fs pump pulse as a function of pump intensity. (b) Measured phase shift as a function of energy delivered to the gas jet of monomers.

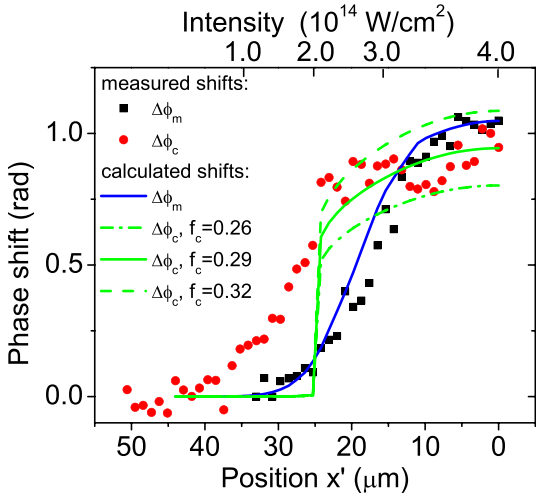

FIG. 11. Measured and calculated phase shifts vs. distance from the laser axis. The blue curve is the calculated $\Delta\phi_m$ based on the ADK model. The green curves are $\Delta\phi_c$ assuming $f_c = 0.26$ (dashed-dotted line), 0.29 (solid line), and 0.32 (dashed line) with the same spatial intensity distribution used to calculate $\Delta\phi_m$.

measured values at high intensities, but there is a significant discrepancy at low intensities ($I_{pu} < 2.0 \times 10^{14}$ W/cm^2, corresponding to positions greater than 25 μm).

This discrepancy is related to the steep rise of Z_c at $I_{pu} = 1.94 \times 10^{14}$ W/cm^2 in our model [see Fig. 10(a)], which in turn makes the calculated Z_c (and thus $\Delta\phi_c$) extremely sensitive to small changes in intensity near this ionization threshold. The actual radial $\Delta\phi_c$ profile is smoother than the calculated green curves in Fig. 11. The threshold shown in Fig. 10(a) is artificially sharp because of simplifying assumptions of our reduced model. An enhanced field E_c within the cluster is primarily responsible for this sharp threshold. As the instantaneous laser intensity rises, N_e sweeps upward through $3N_{crit}$, causing a resonance that briefly enhances E_c [as illustrated in Fig. 12(a)] as well as tunneling and collisional ionization rates [as shown in Fig. 12(b)]. However, our reduced code exaggerates this effect because it assumes a uniform electron density profile. Consequently, the field is enhanced globally throughout the cluster, whereas even a slight density non-uniformity localizes the field enhancement in a layer where $N_e = N_{crit}$, greatly diminishing its effect.[55] Inaccurate description of the cluster ionization threshold is thus a minor disadvantage of our reduced code compared to a full MPIC code. However, as long as I_{pu} substantially exceeds this threshold, the brief resonance interval contributes negligibly to the calculated cluster state. For example, for a 40 fs pump pulse with $I_{pu} = 4 \times 10^{14}$ W/cm^2, Z_c before expansion changes only from 2.50 to 2.54 if we introduce a constraint of $E_c \leq E_{ext}$ to prevent field enhancement, while T_e is unaffected.

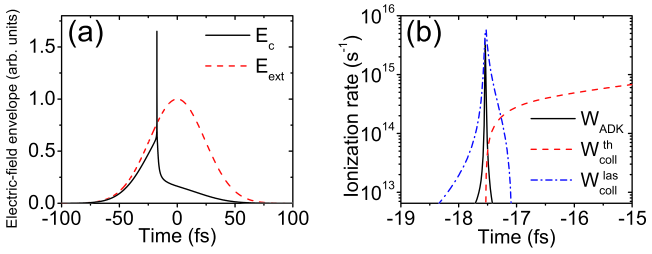

FIG. 12. (a) Envelope of the field inside the cluster and externally applied field (field of the laser). (b) Rates of ADK ionization W_{ADK} (solid black), collisional ionization by thermal electrons W^{th}_{coll} (dashed red), and collisional ionization by quivering electrons W^{las}_{coll} (dashed-dotted blue) for Ar $\rightarrow$ Ar$^+$ during the time of field enhancement. The calculation is done for a laser pulse with $I_{pu} = 4 \times 10^{14}$ W/cm^2, $\lambda = 800$ nm, $\tau_p = 40$ fs.

C. Parameter scans

In this section, we present measurements for a wide range of experimental conditions, including scans of delay time t, distance x from the jet axis, backing pressure P_0, and reservoir temperature T_0 of the gas jet. The cluster fraction $\bar{f}_c$ was calculated for the axial line-out of the reconstructed phase shift using the results $Z_m = 1$ and $Z_c = 2.24$ for our pumping conditions from the analysis of Sec. II. The parameter scans presented here are intended to illustrate the versatility and limitations of the FDH "two-step" method in measuring $\bar{f}_c$ under various conditions. They are not intended as comprehensive scans of the entire parameters space of pulsed supersonic jets.

Figure 13(a) shows time-resolved axial phase shifts $\Delta\phi_{pr}(\tau)$ for backing pressure 34 bar measured at a fixed location $z \approx 1$ mm downstream from the nozzle and $x \sim 1.5$ mm from the jet axis at several times t after the valve opened. The valve closed at $t = 0.8$ ms. Each curve in Fig. 13(a) is an average of 20 single-shot time-resolved phase shifts, but $\bar{f}_c$ was extracted for each shot. Fig 13(b) plots the average and standard deviation of $\bar{f}_c$ for these 20 shots as a function of t. Gas jet and laser fluctuations and data noise were responsible for shot-to-shot variations in the time-resolved phase shifts. The evolution of $\bar{f}_c(t)$ differs substantially from $N_{tot}(t)$. In contrast to $\bar{f}_c(t)$, N_{tot} rises sharply in the interval $0.1 < t < 0.3$ ms, as can be seen from the difference in phase shift between the $t = 0.1$ ms (black squares) and $t = 0.3$ ms (red circles) curves in Fig. 13(a). Moreover, N_{tot} drops substantially in the interval $0.8 < t < 1.0$ ms immediately after the valve closes, as can be seen from the difference between the $t = 0.8$ ms (green down triangles) and $t = 1.0$ ms (lavender left triangles) curves in Fig. 13(a), whereas $\bar{f}_c$ remains high. Thus, $\bar{f}_c(t)$ does not track, and cannot be inferred from $N_{tot}(t)$, but requires an independent measurement.

Figures 14(a) and 14(b) show the time-resolved axial phase shifts $\Delta\phi_{pr}(\tau)$ and $\bar{f}_c$ as a function of the position x for

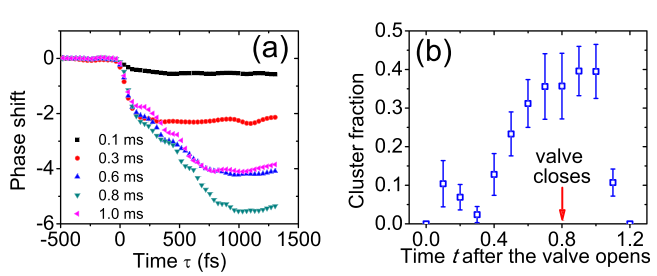

FIG. 13. (a) Time-resolved phase shifts $\Delta\phi_{pr}(\tau)$ at different times t after the valve of the gas jet opens. Each curve is an average of 20 shots. (b) Average cluster fraction $\bar{f}_c$ vs. time t. Each data point represents the average of 20 shots. The error bar shows the standard deviation. The red arrow indicates the time when the valve closed.

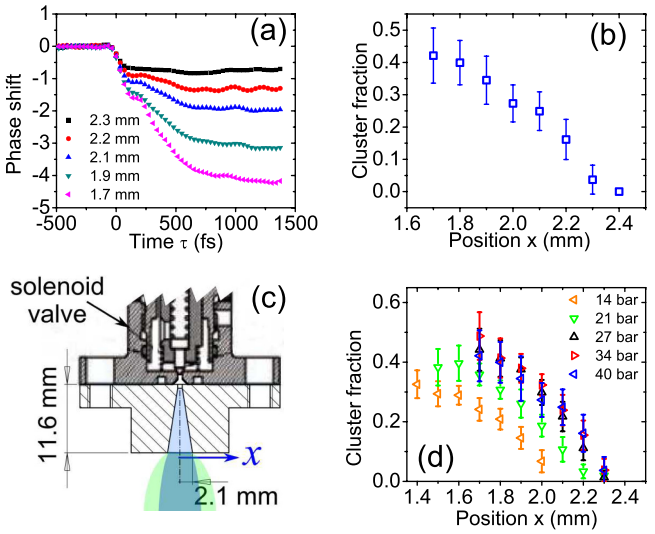

FIG. 14. (a) Time-resolved phase shifts $\Delta\phi_{\rm pr}(\tau)$ at various distances x from the jet axis ($P_0 = 40$ bar, $t = 1$ ms). Each curve is an average of 20 single-shot measurements. (b) Average cluster fraction $\bar{f}_c$ vs. position x. (c) A schematic of gas expansion. The green region represents the monomer beam and the blue region represents the cluster beam. (d) Cluster fraction $\bar{f}_c$ vs. position x at several pressures.

backing pressure $P_0 = 40$ bar at $t = 1$ ms after the valve opens. The valve closed at $t = 1.2$ ms for these data. The vertical position is ~1 mm downstream from the nozzle, of which the exit radius is 2.1 mm, as shown in Fig. 14(c). The plot is limited to $x \gtrsim 1.5$ mm because that is where the strongest variation $\bar{f}_c(x)$ is observed. In addition, for $x < 1.5$ mm, the "step" that separates the $\Delta\phi_m$ and $\Delta\phi_c$ stages of the $\Delta\phi_{pr}(\tau)$ evolution sometimes became difficult to observe with our current τ resolution because of the steep initial slope of the $\Delta\phi_c$ stage at high $\bar{f}_c$, and because strong probe absorption weakened the signal and thus increased noise level. These technical limits, however, are not fundamental and can probably be improved by increasing τ resolution and signal averaging. $\bar{f}_c$ decreases sharply for distances $x > 1.5$ mm from the jet center. Clusters nearly vanish at $x = 2.3$ mm, even though monomer density remains substantial, as indicated by the phase shift at $x = 2.3$ mm (black squares) in Fig. 14(a). A similar positional dependence of $\bar{f}_c$ is observed over a range of backing pressures, as shown in Fig. 14(d). This concentration of heavy clusters near the core of the jet resembles radial mass separations that have been observed in supersonic jets of mixed monomer gas species.[56] In the latter case, the concentration of the heavier species near the center of the jet was attributed to the greater radial thermal velocity and greater diverging angle of the lighter species as the gas expands. Quantitative diffusive separation theory was later developed in the limit of weak viscosity[57] and was confirmed in experiment.[58] Similarly, in our case, monomers expand more rapidly in the radial direction, creating an annular fringe of low cluster fraction, as shown schematically in Fig. 14(c). Simulations that model cluster condensation as an inviscid flow lack this radial dependence, instead showing homogeneous f_c and r_c across the jet.[23] Our result therefore suggests that diffusive separation would be a necessary element of a simulation of cluster formation that captures this radial variation. Our result also suggests that $\bar{f}_c$ on the jet axis would increase a long distance from the nozzle, because of the greater divergence of monomers. This may be the reason for the high cluster fraction ($f_c = 0.9$) measured meters away from the nozzle.[16]

Figure 15 shows (a) the time-resolved axial phase shifts $\Delta\phi_{\rm pr}(\tau)$ and (b) $\bar{f}_c$ as a function of backing pressure P_0, using data at $x = 1.7$ mm from Fig. 14(d). At this location x and time $t = 1$ ms, $\bar{f}_c$ increases monotonically for $P_0 < 34$ bar, then saturates at higher pressure. A similar trend in $\bar{f}_c(P_0)$ was observed in molecular clustered gases using Raman scattering.[21] Close inspection of Fig. 15(a) suggests that $\bar{f}_c = N_{\#}N_c/N_{\rm tot}$ increases with P_0 primarily because cluster radius $r_c \propto N_{\#}^{1/3}$ increases at the expense of monomer density. Increasing r_c is evident from the increasing time ($\Delta\tau$) required for the second step of the phase shift evolution in Fig. 15(a) to reach steady state level—i.e., the cluster expansion time. This time, which scales approximately as r_c (and thus as $N_{\#}^{1/3}$), roughly doubles from 14 bar to 34 bar, implying that $N_{\#}$ increases ~8-fold. Confirming this estimate, Hagena's scaling law[15] modified for our conditions[29] predicts that r_c at 34 bar is 1.7 times its value at 14 bar. Over the same pressure range, $N_{\rm tot}$, which is proportional to $\Delta\phi_m/Z_m + \Delta\phi_c/Z_c$, increases by less than a factor of 2 using $\Delta\phi_m$ and $\Delta\phi_c$ in Fig. 15(a). These numbers easily account for the observed doubling of $\bar{f}_c = N_{\#}N_c/N_{\rm tot}$, and even imply a modest decrease in N_c over the same pressure range. N_c decreases because large clusters grow from coagulation of small clusters.[16] For $P_0 > 34$ bar, the asymptotic phase shift $\Delta\phi_{\rm pr}(\tau = 1.5$ ps) saturates [compare magenta down triangles and blue diamonds in Fig. 15(a)], suggesting that $N_{\rm tot}$ no longer increases with P_0. This may result from pressure-dependent mass redistribution within the jet, combined with the off-center probing position. The scaling law[29] predicts a 10% increase in r_c from 34 bar to 40 bar. This increase may be too small to be clearly seen from cluster expansion time $\Delta\tau$ at 34 and 40 bar.

Figure 16 shows (a) time-resolved axial phase shifts $\Delta\phi_{\rm pr}(\tau)$ and (b) $\bar{f}_c$ as a function of temperature. For these data, a nozzle with 1 mm exit radius ($d = 500\ \mu$m and $\alpha = 5°$) was used to avoid large phase shift at low temperature. The jet was probed at $x \approx 0.8$ mm, $z \approx 1$ mm, and P_0 was kept at 16.5 bar to ensure that clusters were small enough that the phase shift reached its asymptotic value within ~1 ps even at 170 K. To explore higher P_0, one could

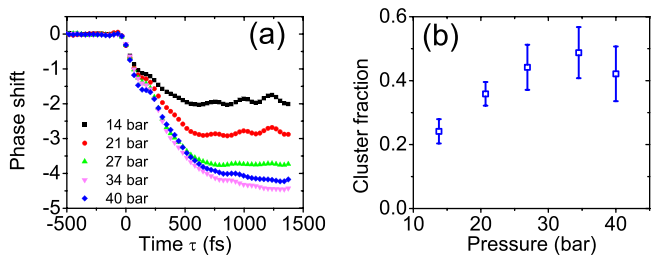

FIG. 15. (a) Time-resolved phase shifts $\Delta\phi_{\rm pr}(\tau)$ at different pressure at $x = 1.7$ mm. Each curve is an average of 20 single-shot measurements. (b) Average cluster fraction $\bar{f}_c$ vs. pressure. $\bar{f}_c$ was extracted from each shot. Each data point represents the average of 20 shots. The error bar is the standard deviation.

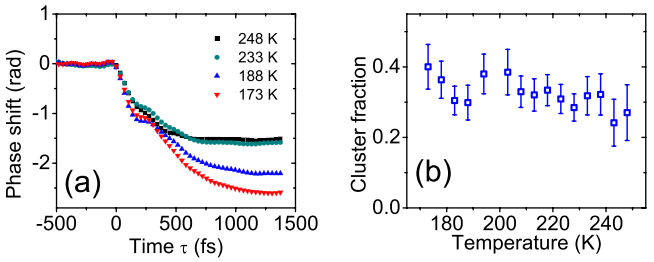

FIG. 16. (a) Time-resolved phase shifts $\Delta\phi_{pr}(\tau)$ at various temperatures. Each curve is an average of 40 single-shot measurements. (b) Average cluster fraction $\bar{f}_c$ vs. temperature. $\bar{f}_c$ was extracted from each shot. Each data point represents the average of 40 shots. The error bar is the standard deviation.

increase I_{pu} to reduce cluster expansion time, or use longer chirped probe and reference pulses. The cooling system required a long time to reach a stable temperature after we adjusted the coolant flow rate. Thus, for convenience, we stopped the coolant after the valve reached 170 K, then let the temperature rise slowly. The temperature rose less than 1 K during the time for acquiring data from 40 shots. As temperature rose from 173 K to 233 K, two trends were observed. First, cluster size decreased. This is evident from the decreased cluster expansion time $\Delta\tau$ between the 173 K (red down triangles) and 233 K (green circles) data in Fig 16(a). Moreover, according to the modified Hagena scaling law,[29] cluster radius at 233 K is 2/3 its value at 177 K. Second, $\bar{f}_c$ decreased slightly from ~0.4 to ~0.3, and eventually to ~0.25 at 248 K. Thus for the conditions considered here, $\bar{f}_c$ depends weakly on temperature. Nevertheless, in future work, it will be important to explore whether $\bar{f}_c$ values approaching unity are achievable when low temperature is combined with higher P_0, more central probing positions x, and optimized probing time t.

Our pressure and temperature scans taken together show generally that $\bar{f}_c$ increases (or saturates) as Γ^*, and thus r_c, increases, qualitatively consistent with other experiments and simulations.[17,23] This relationship, and its dependence on x, z, and t, should also be documented more quantitatively in future work.

IV. SUMMARY

We have determined the cluster mass fraction in a supersonic argon jet by measuring femtosecond evolution of the jet's refractive index by single-shot frequency domain holography. To interpret the measurements, the cluster mass fraction was calculated using a model for asymptotic average charge states of clusters and monomers. The model has been benchmarked against the experimental data and MPIC simulation and shows reasonable agreement for pump pulse intensity significantly exceeding 2×10^{14} W/cm^2. Various influences (time t, transverse position x, backing pressure P_0, temperature T_0) on cluster mass fraction have been examined. Based on the limited scans presented here, we conclude that the highest cluster mass fraction $\bar{f}_c$ is achieved in the core of the gas jet, ~1 ms after the valve opens, with the highest backing pressure P_0 and lowest temperature available. More comprehensive application of the method presented here can provide a complete spatio-temporal picture of cluster formation dynamics in a wide variety of pulsed supersonic jets. The method also provides fast, *in-situ* measurement of $\bar{f}_c$ at specific locations within a jet that can support a wide variety of high-intensity laser-cluster interaction experiments.

ACKNOWLEDGMENTS

This work was supported by U.S. NSF Grant PHY-0936283 and DOE Grants DE-FG02-96ER40954 and DE-FG02-07ER54945. We acknowledge valuable discussions with B. Breizman, J. Keto, M. Becker, and T. Ditmire.

[1]T. Fennel, K. H. Meiwes-Broer, J. Tiggesbäumker, P. G. Reinhard, P. M. Dinh, and E. Suraud, Rev. Mod. Phys. **82**, 1793 (2010); V. P. Krainov and M. B. Smirnov, Phys. Rep. **370**, 237 (2002).
[2]K. W. Madison, P. K. Patel, D. Price, A. Edens, M. Allen, T. E. Cowan, J. Zweiback, and T. Ditmire, Phys. Plasmas **11**, 270 (2004).
[3]W. Bang, G. Dyer, H. J. Quevedo, A. C. Bernstein, E. Gaul, M. Donovan, and T. Ditmire, Phys. Rev. E **87**, 023106 (2013).
[4]Y. Fukuda, Y. Akahane, M. Aoyama, Y. Hayashi, T. Homma, N. Inoue, M. Kando, S. Kanazawa, H. Kiriyama, S. Kondo, H. Kotaki, S. Masuda, M. Mori, A. Yamazaki, K. Yamakawa, E. Y. Echkina, I. N. Inovenkov, J. Koga, and S. V. Bulanov, Phys. Lett. A **363**, 130 (2007).
[5]L. Zhang, L.-M. Chen, W.-M. Wang, W.-C. Yan, D.-W. Yuan, J.-Y. Mao, Z.-H. Wang, C. Liu, Z.-W. Shen, A. Faenov, T. Pikuz, D.-Z. Li, Y.-T. Li, Q.-L. Dong, X. Lu, J.-L. Ma, Z.-Y. Wei, Z.-M. Sheng, and J. Zhang, Appl. Phys. Lett. **100**, 014104 (2012).
[6]Y. Fukuda, A. Y. Faenov, M. Tampo, T. A. Pikuz, T. Nakamura, M. Kando, Y. Hayashi, A. Yogo, H. Sakaki, T. Kameshima, A. S. Pirozhkov, K. Ogura, M. Mori, T. Z. Esirkepov, J. Koga, A. S. Boldarev, V. A. Gasilov, A. I. Magunov, T. Yamauchi, R. Kodama, P. R. Bolton, Y. Kato, T. Tajima, H. Daido, and S. V. Bulanov, Phys. Rev. Lett. **103**, 165002 (2009).
[7]T. D. Donnelly, T. Ditmire, K. Neuman, M. D. Perry, and R. W. Falcone, Phys. Rev. Lett. **76**, 2472 (1996).
[8]C. Vozzi, M. Nisoli, J. P. Caumes, G. Sansone, S. Stagira, S. De Silvestri, M. Vecchiocattivi, D. Bassi, M. Pascolini, L. Poletto, P. Villoresi, and G. Tondello, Appl. Phys. Lett. **86**, 111121 (2005).
[9]H. Ruf, C. Handschin, R. Cireasa, N. Thiré, A. Ferré, S. Petit, D. Descamps, E. Mével, E. Constant, V. Blanchet, B. Fabre, and Y. Mairesse, Phys. Rev. Lett. **110**, 083902 (2013).
[10]R. A. Ganeev, L. B. E. Bom, and T. Ozaki, J. Appl. Phys. **106**, 023104 (2009).
[11]F. Dorchies, F. Blasco, C. Bonté, T. Caillaud, C. Fourment, and O. Peyrusse, Phys. Rev. Lett. **100**, 205002 (2008).
[12]B. Landgraf, M. Schnell, A. Sävert, M. C. Kaluza, and C. Spielmann, Rev. Sci. Instrum. **82**, 083106 (2011).
[13]K. Y. Kim, V. Kumarappan, and H. M. Milchberg, Appl. Phys. Lett. **83**, 3210 (2003).
[14]S. Jinno, Y. Fukuda, H. Sakaki, A. Yogo, M. Kanasaki, K. Kondo, A. Y. Faenov, I. Y. Skobelev, T. A. Pikuz, A. S. Boldarev, and V. A. Gasilov, Appl. Phys. Lett. **102**, 164103 (2013).
[15]O. F. Hagena, Rev. Sci. Instrum. **63**, 2374 (1992).
[16]J. M. Soler, N. García, O. Echt, K. Sattler, and E. Recknagel, Phys. Rev. Lett. **49**, 1857 (1982).
[17]J. Wörmer, V. Guzielski, J. Stapelfeldt, and T. Möller, Chem. Phys. Lett. **159**, 321 (1989).
[18]U. Buck and R. Krohne, J. Chem. Phys. **105**, 5408 (1996).
[19]J. Farges, M. F. Deferaudy, B. Raoult, and G. Torchet, J. Chem. Phys. **84**, 3491 (1986).
[20]E. Fort, F. Pradere, A. De Martino, H. Vach, and M. Chatelet, Eur. Phys. J. D **1**, 79 (1998).
[21]A. Ramos, J. M. Fernandez, G. Tejeda, and S. Montero, Phys. Rev. A **72**, 053204 (2005).
[22]Y. M. Chen, M. Y. Hsu, Y. H. Hsieh, J. Y. Lin, J. Wang, and S. Y. Chen, Opt. Lett. **32**, 2714 (2007).
[23]A. S. Boldarev, V. A. Gasilov, A. Y. Faenov, Y. Fukuda, and K. Yamakawa, Rev. Sci. Instrum. **77**, 083112 (2006).

[24]M. A. Ratner, Low Temp. Phys. **25**, 266 (1999).
[25]Z. Li, J. Zhong, and D. A. Levin, J. Phys. Chem. C **114**, 5276 (2010).
[26]B. Shim, G. Hays, R. Zgadzaj, T. Ditmire, and M. C. Downer, Phys. Rev. Lett. **98**, 123902 (2007).
[27]K. Y. Kim, I. Alexeev, E. Parra, and H. M. Milchberg, Phys. Rev. Lett. **90**, 023401 (2003).
[28]C. Prigent, C. Deiss, E. Lamour, J.-P. Rozet, D. Vernhet, and J. Burgdoerfer, Phys. Rev. A **78**, 053201 (2008).
[29]F. Dorchies, F. Blasco, T. Caillaud, J. Stevefelt, C. Stenz, A. S. Boldarev, and V. A. Gasilov, Phys. Rev. A **68**, 023201 (2003).
[30]K. L. Saenger and J. B. Fenn, J. Chem. Phys. **79**, 6043 (1983).
[31]J. W. Keto, H. Cai, M. Kykta, C. Lei, T. Moller, and G. Zimmerer, J. Chem. Phys. **107**, 6080 (1997).
[32]Y. Fukuda, K. Yamakawa, Y. Akahane, M. Aoyama, N. Inoue, H. Ueda, J. Abdallah, G. Csanak, A. Y. Faenov, A. I. Magunov, T. A. Pikuz, I. Y. Skobelev, A. S. Boldarev, and V. A. Gasilov, JETP Lett. **78**, 115 (2003).
[33]G. Chen, B. Kim, B. Ahn, and D. E. Kim, J. Appl. Phys. **106**, 053507 (2009).
[34]G. Chen, X. Geng, H. Xu, Y. Mi, X. Zhang, L. Wang, and D. E. Kim, AIP Adv. **3**, 032133 (2013).
[35]X. Gao, X. Wang, B. Shim, A. V. Arefiev, R. Korzekwa, and M. C. Downer, Appl. Phys. Lett. **100**, 064101 (2012).
[36]A. V. Arefiev, X. Gao, M. R. Tushentsov, X. Wang, B. Shim, B. N. Breizman, and M. C. Downer, High Energy Density Phys. **6**, 121 (2010).
[37]W. Christen, T. Krause, B. Kobin, and K. Rademann, J. Phys. Chem. A **115**, 6997 (2011).
[38]M. V. Ammosov, N. B. Delone, and V. P. Krainov, Sov. Phys. JETP **64**, 1191 (1986).
[39]M. P. F. Bristow and I. I. Glass, Phys. Fluids **15**, 2066 (1972).
[40]A. Arefiev, B. Breizman, V. Khudik, X. Gao, and M. Downer, Plasma Fusion Res. **5**, S2071 (2010).
[41]W. Lotz, Z. Phys. A: Hadrons Nucl. **216**, 241 (1968).
[42]J. C. Stewart and K. D. Pyatt, Jr., Astrophys. J. **144**, 1203 (1966).
[43]P. Hilse, M. Moll, M. Schlanges, and T. Bornath, Laser Phys. **19**, 428 (2009).
[44]T. Ditmire, T. Donnelly, A. M. Rubenchik, R. W. Falcone, and M. D. Perry, Phys. Rev. A **53**, 3379 (1996).
[45]J. Zweiback, *Resonance Effects in Laser Cluster Interactions*, Ph.D. dissertation (University of California, Davis, 1999). A sign typo in the expression of W_{1as} was corrected there.
[46]A. V. Gurevich and L. P. Pitaevskii, Sov. Phys. JETP **19**, 870 (1964).
[47]J. Meyer-ter Vehn, A. Tronnier, and Y. Cang, in *35th EPS Conference on Plasma Physics, Hersonissos, 9–13 June* (2008), ECA Vol. 32D, P2.132.
[48]R. Ramis, K. Eidmann, J. Meyer-ter Vehn, and S. Hueller, Comput. Phys. Commun. **183**, 637 (2012).
[49]J. Farges, M. de Feraudy, B. Raoult, and G. Torchet, Surf. Sci. **106**, 95 (1981); O. G. Danylchenko, Y. S. Doronin, S. I. Kovalenko, and V. N. Samovarov, JETP Lett. **84**, 324 (2006).
[50]For $10^3 \lesssim N_{\#} \lesssim 10^5$, argon clusters are a mixture of fcc, hcp and random close-packed structures. See, for example, B. W. van de Waal, G. Torchet, and M.-F. de Feraudy, Chem. Phys. Lett. **331**, 57 (2000).
[51]M. Krishnamurthy, J. Jha, D. Mathur, C. Jungreuthmayer, L. Ramunno, J. Zanghellini, and T. Brabec, J. Phys. B **39**, 625 (2006).
[52]M. Takeda, H. Ina, and S. Kobayashi, J. Opt. Soc. Am. **72**, 156 (1982).
[53]S. P. Le Blanc, E. W. Gaul, N. H. Matlis, A. Rundquist, and M. C. Downer, Opt. Lett. **25**, 764 (2000).
[54]K. Y. Kim, I. Alexeev, and H. M. Milchberg, Appl. Phys. Lett. **81**, 4124 (2002).
[55]H. M. Milchberg, S. J. McNaught, and E. Parra, Phys. Rev. E **64**, 056402 (2001).
[56]P. C. Waterman and S. A. Stern, J. Chem. Phys. **31**, 405 (1959).
[57]F. S. Sherman, Phys. Fluids **8**, 773 (1965).
[58]D. E. Rothe, Phys. Fluids **9**, 1643 (1966).